Generation and measurement of intense few-femtosecond superradiant extreme-ultraviolet free-electron laser pulses

Najmeh S. Mirian[1,2], Michele Di Fraia[1], Simone Spampinati[1], Filippo Sottocorona[1,3], Enrico Allaria[1,2], Laura Badano[1], Miltcho B. Danailov[1], Alexander Demidovich[1], Giovanni De Ninno[1,4], Simone Di Mitri[1], Giuseppe Penco[1], Primož Rebernik Ribič[1,4], Carlo Spezzani[1], Giulio Gaio[1], Mauro Trovó[1], Nicola Mahne[1], Michele Manfredda[1], Lorenzo Raimondi[1], Marco Zangrando[1,5], Oksana Plekan[1], Kevin C. Prince[1,6], Tommaso Mazza[7], Richard J. Squibb[8], Carlo Callegari[1], Xi Yang[9] and Luca Giannessi[1,10] ✉

Free-electron lasers producing ultrashort pulses with high peak power promise to extend ultrafast non-linear spectroscopic techniques into the extreme-ultraviolet–X-ray regime. Key aspects are the synchronization between pump and probe, and the control of the pulse properties (duration, intensity and coherence). Externally seeded free-electron lasers produce coherent pulses that can be synchronized with femtosecond accuracy. An important goal is to shorten the pulse duration, but the simple approach of shortening the seed is not sufficient because of the finite-gain bandwidth of the conversion process. An alternative is the amplification of a soliton in a multistage, superradiant cascade: here, we demonstrate the generation of few-femtosecond extreme-ultraviolet pulses, whose duration we measure by autocorrelation. We achieve pulses four times shorter, and with a higher peak power, than in the standard high-gain harmonic generation mode and we prove that the pulse duration matches the Fourier transform limit of the spectral intensity distribution.

Free-electron lasers (FELs) capable of generating intense few-femtosecond pulses from the extreme ultraviolet (EUV) to the soft-X-ray region are opening a wide range of new scientific opportunities. This timescale allows the probing of ultrafast, out-of-equilibrium dynamics and the high intensities are key for non-linear optics. Soft-X-ray wavelengths can access core electrons of the extremely important light elements carbon, nitrogen and oxygen, providing chemical sensitivity; fast pulses can drive the system under study into a regime where the transient excitation is not depleted by competing fast channels, such as Auger decay[1]. The 1*s* core holes of low-*Z* elements and the 2*p* core holes of many light transition metals have lifetimes in this range, and are invaluable for probing carrier interactions and charge-transfer processes in many solids and molecules[2–4]. Ultrashort pulses can probe terahertz-driven dynamics, such as coherent phonons or collective excitations in condensed matter, opening the way to the observation of field-dependent, coherently driven phenomena[5,6].

Most pump–probe experiments with FELs must cope with the many complications of poor synchronization and large intensity fluctuations: the need for post-processing; the rejection of outliers reducing the efficiency of data collection; and rogue pulses that may be the cause of premature sample damage. Externally seeded FELs, currently based on high gain harmonic generation (HGHG), are ideal in terms of synchronization (a few femtoseconds (ref. [7])) and control of pulse properties, which are inherited from the seed source[8–10]. The typical pulse duration, in a seeded HGHG FEL, is a function of the seed duration and decreases with harmonic order[11]; at the FERMI machine used in this study, two HGHG FELs cover the range from 100 to 4 nm (refs. [8,12]), with pulses from 90 fs down to 20 fs (for a 70 fs seed). Shorter pulses are currently a high priority worldwide and could be obtained by reducing the duration of the seed pulse to the limit imposed by the bandwidth of the conversion/amplification process; various strategies based on shaping the FEL gain bandwidth have been proposed in refs. [13–17]. Most other methods are based on the manipulation of electron beam properties such as the emittance, beam current, energy spread, or trajectory, or optical functions[18–26]. All these techniques share the common constraint associated with the finite-gain bandwidth of the FEL process, which at EUV wavelengths restricts the pulse duration to values above 10 fs, a minimum requirement to resolve the nuclear dynamics of light elements, or to approach the lifetime of Auger decay in core-hole excitations.

An alternative, which exploits the FEL dynamic process itself to beat the gain bandwidth limit, was proposed in ref. [27]: driving the FEL amplifier into saturation and superradiance, along a cascade of undulators resonant at progressively higher harmonics of an initial seed. This is the practical realization of an idealized condition under which a radiation pulse at the onset of saturation in a

[1]Elettra - Sincrotrone Trieste, Trieste, Italy. [2]Deutsches Elektronen-Synchrotron DESY, Hamburg, Germany. [3]Università degli Studi di Trieste, Trieste, Italy. [4]Laboratory of Quantum Optics, University of Nova Gorica, Nova Gorica, Slovenia. [5]Istituto Officina dei Materiali IOM-CNR, Trieste, Italy. [6]Centre for Translational Atomaterials, Swinburne University of Technology, Melbourne, Victoria, Australia. [7]European XFEL, Schenefeld, Germany. [8]University of Gothenburg, Gothenburg, Sweden. [9]National Synchrotron Light Source II, Brookhaven National Laboratory, Upton, NY, USA. [10]Istituto Nazionale di Fisica Nucleare, Laboratori Nazionali di Frascati, Frascati, Italy. ✉e-mail: luca.giannessi@elettra.eu

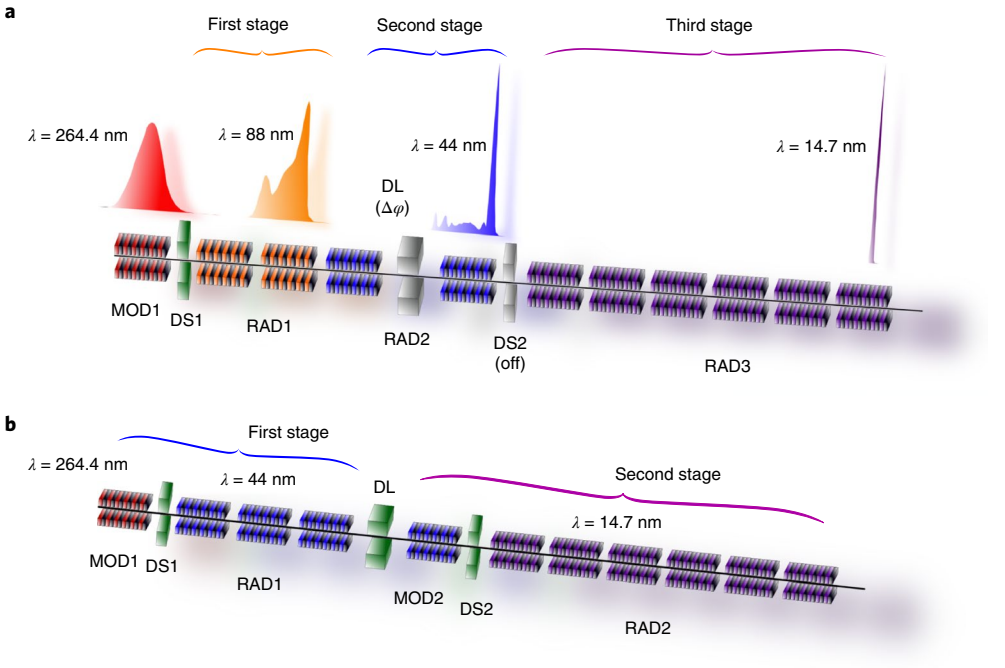

Fig. 1 | FEL layout. a, FEL-2 in SRC mode. The configuration consists of a sequence of FEL amplifiers (radiators RAD1, RAD2 and RAD3), each resonant at a (low-order) harmonic of the previous amplifier in the sequence. The modulator MOD1, resonant with the UV seed laser and separated from the first radiator RAD1 by the dispersive element (DS1), initiates the sequence. The seed intensity and dispersion are tuned to reach saturation at the exit of RAD1. The delay line (DL), set at low current (2.6 A), plays the part of a phase shifter ($\Delta\varphi$) between the two undulators that compose RAD2. MOD1 is set in linear polarization; RAD1–3 are in circular polarization. The temporal pulse envelope at the exit of each stage is shown (see Fig. 4, below). **b**, FEL-2 in the nominal double-stage HGHG cascade mode. The configuration is tuned to reach the same final wavelength of 14.7 nm ($h\nu = 84.34$ eV). Each stage consists of a modulator (MOD1, MOD2), a dispersive section (DS1, DS2) and a set of undulators (collectively: a radiator RAD1, RAD2). At the exit of the first stage, a magnetic delay line shifts the FEL radiation to a fresh portion of the electron bunch, to seed the second stage in the modulator MOD2, and the harmonic conversion process is repeated; polarizations are as in **a**.

FEL amplifier propagates and grows as a self-similar solitary wave, undergoing longitudinal compression[28,29]. After saturation, the peak power of an isolated spike moving along a uniform electron beam grows proportionally to the square of the distance covered along the undulator and its duration becomes shorter than the duration supported by the FEL gain bandwidth at the Fourier transform limit (FTL)[30]. A few experiments carried out at visible wavelengths have demonstrated some of the key elements of the scheme[31–33]. The concept of superradiance is based on a radiation pulse propagating over fresh electrons; the demonstration of multiple-stage conversion implicitly proves the principle that the cascade can be iterated indefinitely, provided that the resonance properties and the amplification conditions remain fulfilled. We have realized a three-stage superradiant cascade (that we label SRC) according to the scheme proposed in ref. [27], starting from an ultraviolet (UV) seed pulse and reaching the EUV spectral range. These measurements quantitatively confirm some key aspects of the theory of superradiant FELs, such as the duration of the superradiant spike, namely that it corresponds to the FTL of the spectral distribution[30]. Finally, we measured and compared the gain spectrum of the FEL in SRC and in a typical HGHG configuration. The analysis of the spectra in SRC has shown an unexpected behaviour consisting of a substantial 'frequency-pulling'[34] effect, which is normally barely observed in HGHG mode[35].

Results

The experiments were carried out at FERMI over three experimental sessions. During the first session, over a short period of eight hours, we compared the duration, energy and spectrum of a pulse at the same target wavelength in SRC mode versus the standard HGHG mode, thus avoiding any difference that might arise from drift in the accelerator performance. The wavelength (14.7 nm) was chosen to be attainable from the seed (264.4 nm) as a triple harmonic jump, $3\times2\times3$. Figure 1b shows the standard two-stage HGHG cascade, tuned to reach the final wavelength in a double harmonic jump (6×3). Figure 1a shows the FEL-2 layout as modified for SRC operation: the first two sections were arranged into an additional frequency-conversion stage at 88 nm, to initiate the cascade with a shorter gain length and longer slippage (the difference between the distance covered by light and electrons while traversing an undulator segment); the dispersive section DS2 was set to zero and the delay line was used as a phase shifter to match the phase between the two second-stage undulators at 44 nm. The switching between the two configurations entailed tuning of the undulator gaps and dispersive sections, while preserving the same electron beam properties and seed duration.

It is common practice to infer the pulse duration indirectly, from more easily measurable parameters and theoretical models (refs. [11,36] and references therein), because a direct measurement is very demanding[37]. The experiment was designed to include an autocorrelation measurement, to provide direct evidence of the pulse duration and to demonstrate that the spectral width of the pulse is a reliable indicator of its duration. We passed the FEL pulse through the FERMI split-and-delay line and we monitored the (energy-resolved) photoelectron signal of two-photon above-threshold ionization (ATI) of argon at the low-density matter beamline[38] (see Methods section). We note that the branching ratio of an ATI process at these wavelengths is four to five orders of magnitude lower than the direct single-photon ionization, further aggravated by the insertion losses of the split-and-delay line, indicating that very high sensitivity is required to perform this measurement.

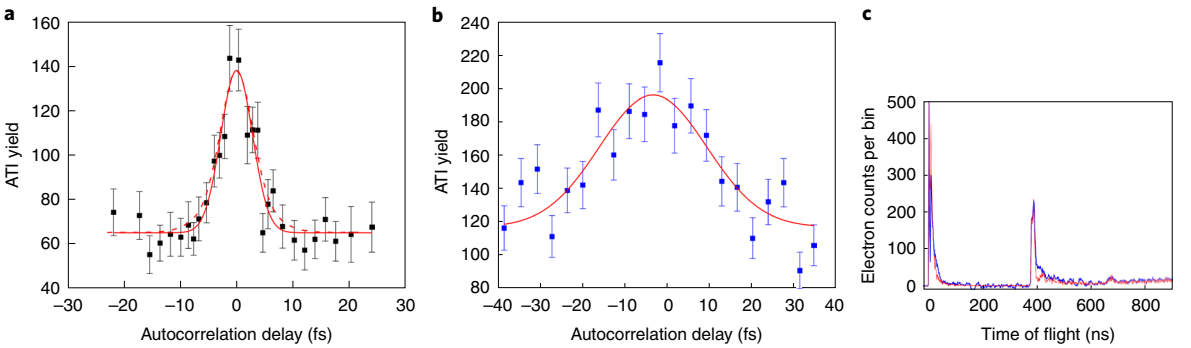

Fig. 2 | Pulse duration. a,**b**, Autocorrelation trace obtained from the argon 3*p* ATI yield (integration of the spectrum in **c** over the time-of-flight window 365–425 ns) with the FEL operating in SRC (**a**) mode and HGHG (**b**) mode. The FWHM of the autocorrelation curves is 6.6 ± 0.9 fs and 31 ± 6 fs respectively, corresponding to a pulse duration (FWHM) of 4.7 ± 0.6 fs and 22 ± 4 fs respectively. Note that the horizontal scale of **a** is expanded with respect to **b** for visual clarity. The red dashed line in **a** is the autocorrelation trace calculated from the simulation in Fig. 4. **c**, Time-of-flight spectrum of the high kinetic energy electrons measured by the magnetic bottle from argon at 84.40 eV FEL photon energy. The electrons are retarded by 70 V, so that no contribution from single-photon processes is detected. The spectrum shows a sharp peak at $t = 0$, corresponding to the photon signal due to scattered photons (used, in fact, to determine $t = 0$). At ~400 ns, corresponding to a kinetic energy (before retardation) of $2h\nu - 15.8$ eV $= 153$ eV, the signature from the ATI of the 3*p* shell of argon is identified. The plot shows both the average of 105,000 analogue traces (in blue) and the histogram (bin size = 1 ns) of the electron counts given by the software discrimination algorithm (in red), with the former normalized to the latter.

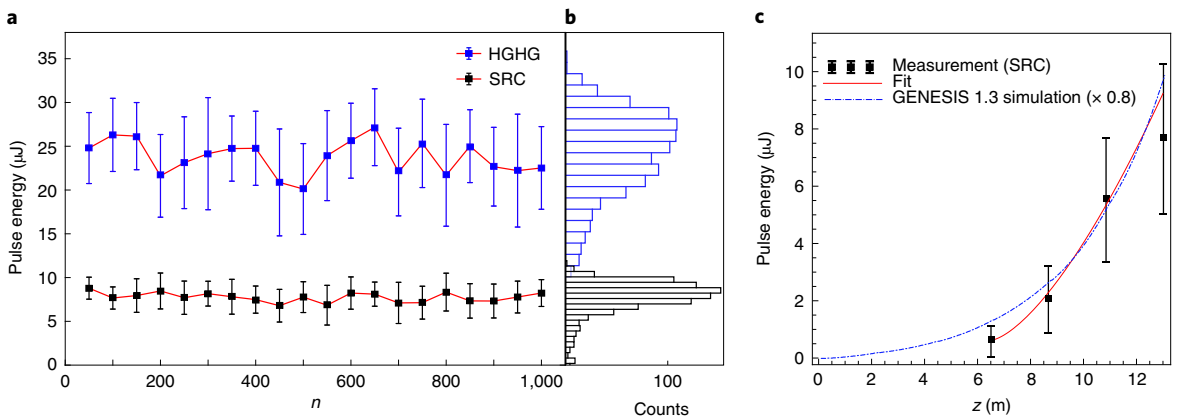

Fig. 3 | Pulse energy. a, Pulse energy measured in a sequence of 1,000 pulses in SRC (red-black) and HGHG (blue-red) modes. At each point, the average value and standard deviation of groups of 50 shots is represented. **b**, Pulse energy histograms of the whole data sample. The pulse energy is measured by the FERMI intensity ionization monitor. The light emitted by the first stages is suppressed by the insertion of a zirconium filter (see Methods). **c**, Pulse energy versus coordinate along the undulator, *z*, in SRC mode: measured (filled black squares, error bars represent the standard deviation of the distribution of 30 samples at each position), GENESIS 1.3 simulation (blue dot-dashed line) and the fit with the scaling function $f(z) = E_0 + \alpha(z - z_0)^{3/2}$ (red solid line), where $z_0 = 6.5$ m, $\alpha = 0.52\ \mu\text{J m}^{-3/2}$ and where the value of $E_0 = 0.62\ \mu$J is set to match the energy measured after the third undulator. The simulation overestimates the measured energy by around 20%.

The autocorrelation traces for the SRC and the HGHG FEL configurations are shown in Fig. 2a,b respectively: the full-width at half-maximum (FWHM) pulse duration derived therefrom is $\delta t_{\text{FEL}} = 4.7 \pm 0.6$ fs in SRC mode, in agreement with the FTL of the experimental spectrum and with the theoretical (GENESIS 1.3) value (see Discussion); in HGHG mode (Fig. 2b) it is 22 ± 4 fs. Figure 2c shows the time-of-flight spectrum of the high-kinetic-energy electrons from argon, measured by the magnetic bottle (see Methods).

The FERMI photon diagnostic system includes an ionization chamber which was used to monitor the pulse energy in the two configurations[39]. Figure 3 shows the pulse energy measured in a sequence of 1,000 consecutive pulses. The averages (±one standard deviation) of the energy distribution were $7.7 \pm 1.8\ \mu$J and $23.5 \pm 5.2\ \mu$J in SRC and HGHG mode respectively; the resulting shot-to-shot relative stability in the two configurations is thus comparable (24% in SRC versus 22% in HGHG). Note that the standard HGHG configuration delivers its larger pulse energy in a longer time, and overall has a lower peak power: ~1 GW versus ~1.5 GW in SRC mode. The energy growth along the radiator was measured, and a comparison with the simulation and with the fitting function $z^{3/2}$ from the third undulator to the end of the line is shown in Fig. 2c.

During the experiment, the radiation spectrum from the three stages was monitored with the FERMI single-shot spectrometer[39]. We acquired and analysed a set of 10^3 FEL spectra both in SRC mode (Fig. 1a) and in the normal HGHG mode (Fig. 1b). The average spectral width, calculated as the FWHM of a Gaussian fit of the power spectrum, was 0.063 ± 0.007 nm and 0.021 ± 0.007 nm for SRC and HGHG respectively. The uncertainty intervals represent the standard deviation of the width distribution. The spectral

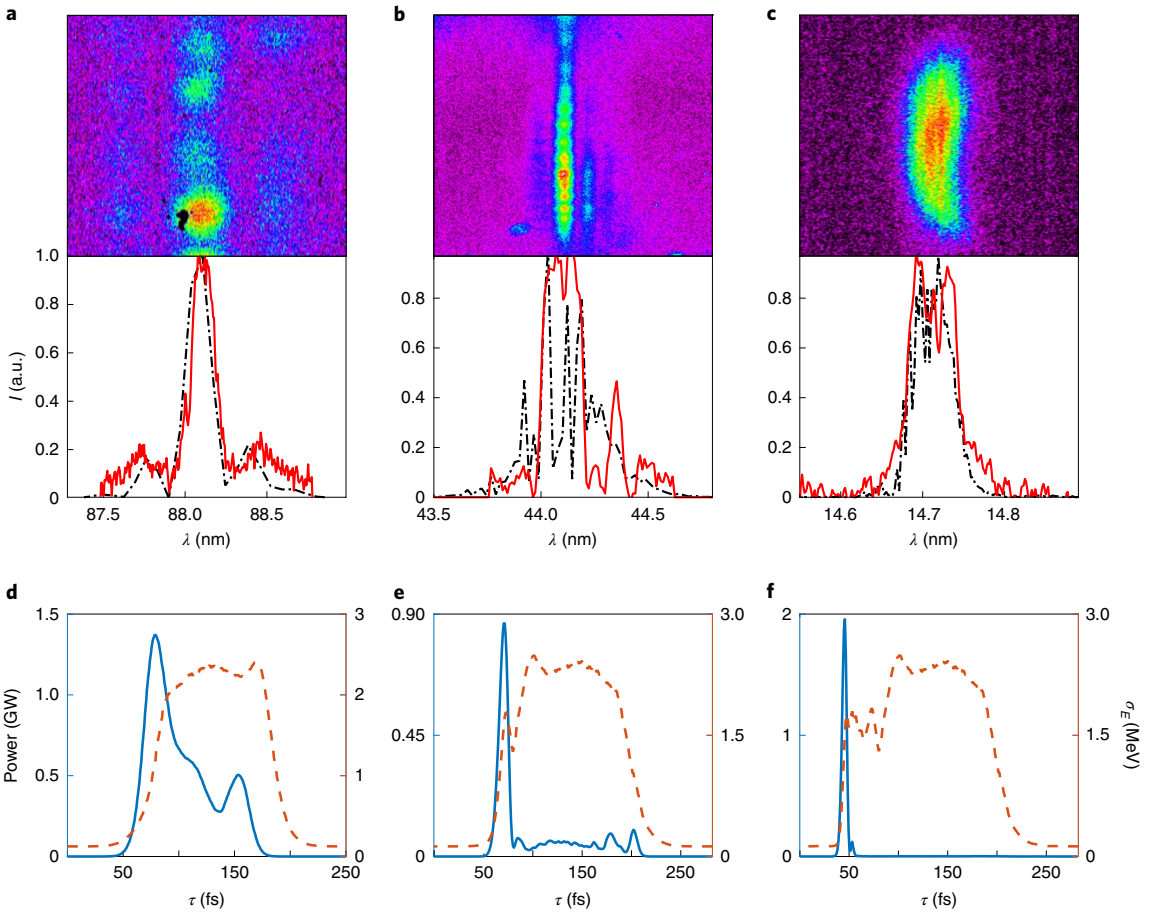

Fig. 4 | Pulse spectrum. a–c, Measured spectra after the first (**a**), second (**b**) and third (**c**) stage. The spectral profiles projected onto the dispersive horizontal axis of the respective raw spectrometer images (red solid line) are compared with the simulated spectral profiles (black dot-dashed line). **d–f**, Simulated radiation intensity profile (blue solid line) and electron beam energy-spread profile (orange dashed line) after the first (**d**), second (**e**) and third (**f**) stage.

width observed in HGHG mode implies an FWHM pulse duration of at least 15 fs (the FTL). This value is smaller than the duration of the measured pulse (22 fs), suggesting the presence of a residual non-linear phase chirp of the seed.

Figure 4a–c shows the measured spectra (single shot) at the exit of the three stages of the cascade (red line). Figure 4d–f shows the results of a simulation at the exit of the same three stages (GENESIS 1.3)[40]. The plots represent the pulse power profile (blue line) and the induced energy spread (orange dashed line); the pulse head is on the left-hand side. The spectra obtained from the simulation are also shown for comparison in Fig. 4a–c (black dot-dashed line). The theory for superradiance predicts that the duration of the superradiant spike can be deduced as the FTL of the spike spectral width[30], in our case: ~5 fs (FWHM), in reasonable agreement with the measurement (Fig. 2a).

During a second experimental session (see Methods and Supplementary Information for details), we measured the FEL spectral behaviour in SRC mode while varying the resonance condition in the final amplifier (Fig. 5a). The seed laser wavelength λ_{seed} and the initial undulator settings are optimized to amplify the harmonic h of the seed, $\lambda_s = \lambda_{seed}/h$; the FEL central emission wavelength λ_p differs slightly from λ_s. The undulator gap and K-parameter data are converted to relative wavelength detuning $(\lambda_g - \lambda_s)/\lambda_s$, where λ_g is the resonant wavelength imposed by the undulator setting, using the standard magnetic calibration of the FERMI undulators. For comparison, a similar measurement was carried out later in a typical HGHG mode (see Supplementary Information) and is shown in Fig. 5b. Each data point represents a sum of 10^3 shots in superradiance mode and 10^2 shots in HGHG mode. In Fig. 5c we show the correlation between the central emission relative wavelength shift $(\lambda_p - \lambda_s)/\lambda_s$ and the undulator relative detuning, in HGHG (black) and SRC (blue) modes. In HGHG mode (black line) we observe the typical behaviour of a modest correlation with a slope

$$\eta = \frac{(\lambda_p - \lambda_s)}{\lambda_g - \lambda_s} \simeq 0.039 \pm 0.035 \qquad (1)$$

and with a decaying intensity while the amplifier is detuned. Conversely, in SRC configuration we have $\eta \simeq 0.91 \pm 0.02$, that is, λ_p closely follows the resonant condition set by the undulator, showing a strong 'frequency-pulling' phenomenon[34].

Discussion

The sidebands in the spectrum of Fig. 4a are the signature of saturation and temporal splitting of the pulse[41–43]; their growth was monitored to tune the seed power (~900 MW) and the dispersive section DS1 ($R_{56} = 60\,\mu m$), to attain the onset of saturation at the exit of the first stage. The same tuning procedure was used in the simulation and resulted in the agreement shown in Fig. 4a. In the second stage (Fig. 4e), the bunched beam radiates at the second harmonic (44 nm). The intensity profile shows a peak on the leading edge, where the bunching is higher and the pulse slips over fresh

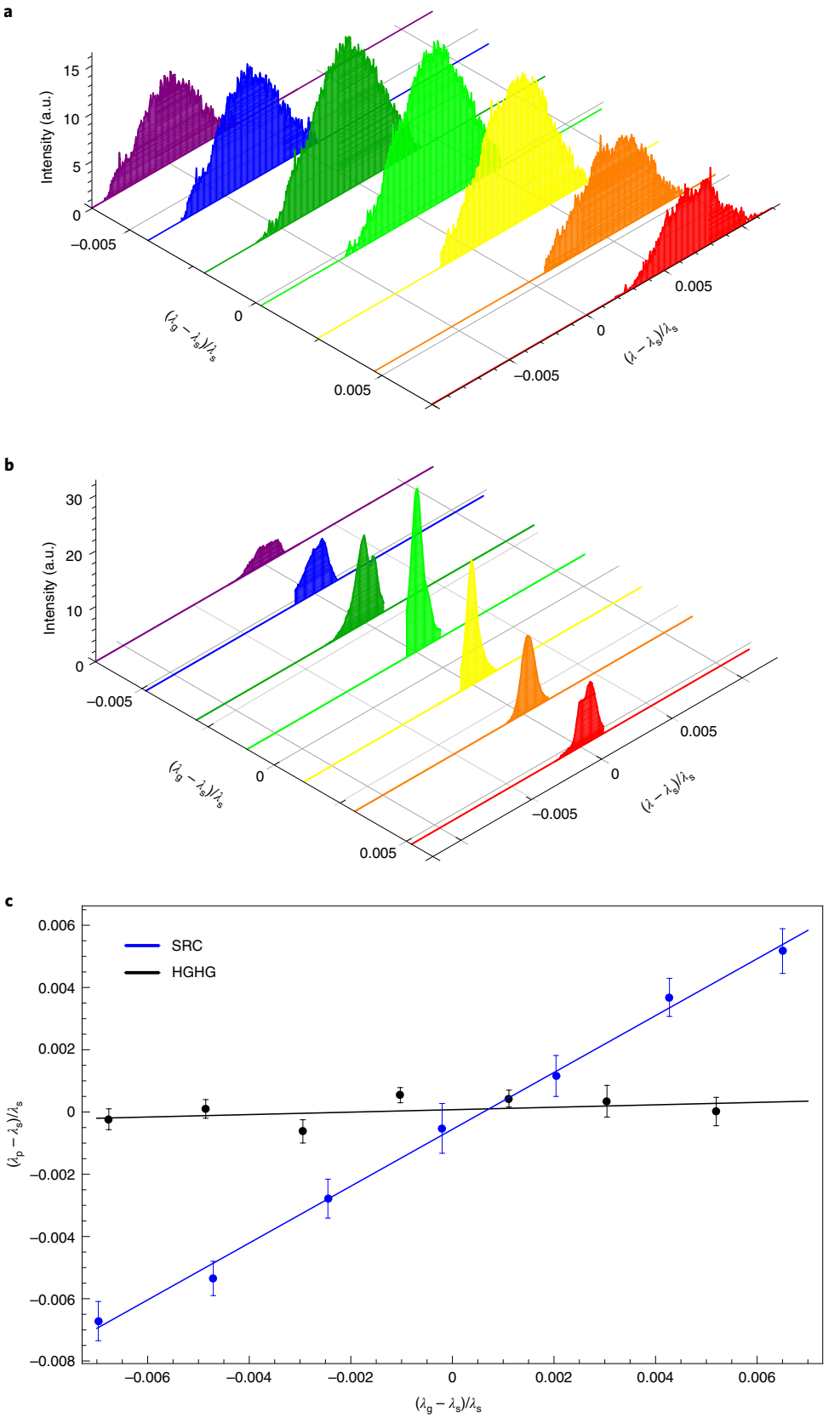

Fig. 5 | Frequency pulling. a, FEL spectrum versus the final amplifier resonant frequency in SRC mode of operation. **b**, FEL spectrum versus the final amplifier resonant frequency in HGHG mode of operation (conversion to harmonic seven in the first stage and three in the second stage). **c**, Central emission frequency versus undulator resonant frequency in HGHG (black) and SRC (blue) mode of operation.

electrons, where the energy spread is not yet affected by the FEL process. The emission in the tail is suppressed by the energy spread accumulated in the previous stage and by the increased sensitivity (due to the shorter wavelength) of the FEL process to the energy spread. Both the measured and the simulated spectra (Fig. 4b) show the formation of sidebands, which result from the interference process between the tail and the main peak. In the last stage (Fig. 4f) the simulation shows a short (5 fs FWHM), intense (2 GW) spike at the pulse leading edge and an essentially complete suppression of the tail; this results in a broad single structure of the simulated spectrum, which is supported by the experimental data (Fig. 4c); note that the sideband structure has disappeared.

To show that the SRC mode can beat the minimum pulse duration supported by the finite FEL gain bandwidth, we compare the latter with the measured value. An indication of the FEL gain bandwidth is given by the FEL parameter $\rho_{\mathrm{FEL}} \simeq \lambda_{\mathrm{u}}/4\pi\sqrt{3}\, l_{\mathrm{g}}$ (ref. [44]), where λ_{u} is the undulator period and $l_{\mathrm{g}} \simeq 1.79$ m is the exponential power folding length (gain length). The latter was estimated by taking the shortest gain length derived from the energy increment between two consecutive undulators in the amplifier and it is consistent with a GENESIS 1.3 simulation of the amplifier starting from shot noise (Supplementary Information). The exponential-gain relative spectral bandwidth for a saturated self-amplified spontaneous emission (SASE) amplifier should therefore be $\rho_{\mathrm{FEL}} \approx 8.9 \times 10^{-4}$. Assuming a transform-limited Gaussian distribution at 14.7 nm, this corresponds to ~10 fs (FWHM): twice the duration measured in SRC mode. Even a simulation of the unseeded amplifier starting from shot noise, that is far from saturation at the end of the amplifier, has a gain bandwidth $\sigma_{\mathrm{g}} \approx 1.6\rho_{\mathrm{fel}}$ and shows a spike duration of 7.7 fs (see Supplementary Information). In SRC mode we therefore produce pulses shorter than those allowed by the gain bandwidth of the corresponding FEL amplifier, while preserving or even exceeding its saturation peak power. Figure 3 shows a comparable pulse energy stability between HGHG and SRC mode. This is a remarkable aspect, since the stability of a SASE amplifier in single-spike mode is characterized by strong shot-to-shot energy fluctuations, an intrinsic characteristic of the chaotic light nature of SASE. These fluctuations are suppressed in seeded FELs[10], and this also applies to the SRC configuration. The dependence of peak power on the square of the distance z along the undulator or the pulse energy scaling as $z^{3/2}$ are a key characteristic of the superradiant pulse evolution[27,30]. Some previous studies, reporting experimental measurement of such energy scaling, considered it as a signature of superradiance[31–33]. Figure 3c shows the pulse energy measured by the ionization monitors while gradually detuning the resonance of the undulators. Starting after the first three undulators the energy growth is well reproduced by a fitting function $\propto z^{3/2}$ (red line). The GENESIS 1.3 simulation shows a trend with similar behaviour (blue dot-dashed line) and provides a pulse energy about 20% higher at the end of the amplification. This could be due to a combination of reasons including non-ideal orbit or matching beam conditions, precision of the simulation and uncertainty in the attenuation of the zirconium filter used to remove contribution from the previous stages (see Methods).

The strong frequency-pulling effect shown in Fig. 5a,c seems to be a distinguishing feature of superradiance. In a seeded FEL, the periodically pre-modulated beam initiating the amplification determines the central emission wavelength λ_{p}. When the gain is detuned by varying the undulator gap in Fig. 5c (black line), we observe the typical HGHG behaviour: the radiation spectrum remains almost centred on the integer harmonic of the seed, that is, $\lambda_{\mathrm{p}} \simeq \lambda_{\mathrm{s}}$. Conversely, in SRC mode (blue line), the central wavelength of emission closely follows the resonant undulator wavelength. This effect is correlated to the bandwidth of the amplification and of the initial condition initiating the process. Let us assume the amplification in the final amplifier as driven by a Gaussian equivalent seed pulse, centred at λ_{s} and with relative spectral width σ_{s}, and a Gaussian FEL gain function centred at the wavelength λ_{g} and relative width σ_{g}. In a linear amplifier, the relative detuning of the FEL emission central wavelength λ_{p}, as a function of λ_{g} would be given by[35],

$$\eta = \frac{\sigma_{\mathrm{s}}^2}{\sigma_{\mathrm{g}}^2 + \sigma_{\mathrm{s}}^2} \tag{2}$$

Inverting equation (2), we estimate the equivalent pulse duration that should start the amplification process. To match the measured value of $\eta = 0.91$, we find $\sigma_{\mathrm{s}} = \sigma_{\mathrm{g}}\sqrt{\frac{\eta}{1-\eta}} \simeq 4.5 \times 10^{-3}$, which corresponds to an FTL equivalent root-mean-square seed duration $\sigma_{\mathrm{t}} \approx 0.86$ fs. In superradiance, the final amplifier behaves as if the amplification were initiated by a pulse as short as a single cycle of the optical seed, a clear difference with the behaviour of HGHG where the modest correlation is consistent with the seed duration predicted by the theory (see Supplementary Information).

In the example presented, we transport light simultaneously from the three stages at 88 nm, 44 nm and 14.7 nm to the experimental chamber. The absence of dispersive sections along the cascade ensures sub-femtosecond-level synchronization also between the different colours, that is, the various harmonics could be phase locked. Pump and probe experiments can be performed, either with a synchronized optical laser or with the EUV light of the intermediate stage (at 44 nm in the example presented here), which is expected to be only around two or three times longer than the measured pulse (see Fig. 4e). On the other hand, single-colour experiments may require filters to suppress the undesired spectral components, a disadvantage that this scheme has in common with the standard double-stage HGHG mode of operation of FEL-2.

The SRC configuration will be implemented soon as one of the operation modes of FERMI for user experiments.

Online content

Any methods, additional references, Nature Research reporting summaries, source data, extended data, supplementary information, acknowledgements, peer review information; details of author contributions and competing interests; and statements of data and code availability are available at https://doi.org/10.1038/s41566-021-00815-w.

Received: 19 April 2020; Accepted: 12 April 2021;
Published online: 17 May 2021

References

1. Schreck, S., Beye, M. & Föhlisch, A. Implications of stimulated resonant X-ray scattering for spectroscopy, imaging, and diffraction in the regime from soft to hard X-rays. *J. Mod. Opt.* **62**, S34–S45 (2015).
2. Calegari, F. et al. Ultrafast electron dynamics in phenylalanine initiated by attosecond pulses. *Science* **346**, 336–339 (2014).
3. Berrah, N. A perspective for investigating photo-induced molecular dynamics from within with femtosecond free electron lasers. *Phys. Chem. Chem. Phys.* **19**, 19536–19544 (2017).
4. Rudenko, A. et al. Femtosecond response of polyatomic molecules to ultra-intense hard X-rays. *Nature* **546**, 129–132 (2017).
5. Bencivenga, F., Capotondi, F., Principi, E., Kiskinova, M. & Masciovecchio, C. Coherent and transient states studied with extreme ultraviolet and X-ray free electron lasers: present and future prospects. *Adv. Phys.* **63**, 327–404 (2015).
6. Prince, K. C. et al. Coherent control with a short-wavelength free-electron laser. *Nat. Photonics* **10**, 176–179 (2016).
7. Danailov, M. B. et al. Towards jitter-free pump-probe measurements at seeded free electron laser facilities. *Opt. Express* **22**, 12869–12879 (2014).
8. Allaria, E. et al. Highly coherent and stable pulses from the FERMI seeded free-electron laser in the extreme ultraviolet. *Nat. Photonics* **6**, 699–704 (2012).
9. De Ninno, G. et al. Single-shot spectro-temporal characterization of XUV pulses from a seeded free-electron laser. *Nat. Commun.* **6**, 8075 (2015).

10. Gorobtsov, O. Y. et al. Seeded X-ray free-electron laser generating radiation with laser statistical properties. *Nat. Commun.* **9**, 4498 (2018).
11. Finetti, P. et al. Pulse duration of seeded free-electron lasers. *Phys. Rev. X* **7**, 021043 (2017).
12. Allaria, E. et al. Two-colour pump–probe experiments with a twin-pulse-seed extreme ultraviolet free-electron laser. *Nat. Commun.* **4**, 2476 (2013).
13. McNeil, B. W. J., Thompson, N. R., Dunning, D. J. & Sheehy, B. High harmonic attosecond pulse train amplification in a free electron laser. *J. Phys. B* **44**, 065404 (2011).
14. Gauthier, D. et al. Chirped pulse amplification in an extreme-ultraviolet free-electron laser. *Nat. Commun.* **7**, 13688 (2016).
15. Tanaka, T. & Rebernic Ribič, P. Shortening the pulse duration in seeded free-electron lasers by chirped microbunching. *Opt. Express* **27**, 30875–30892 (2019).
16. Maroju, P. K. et al. Attosecond pulse shaping using a seeded free-electron laser. *Nature* **578**, 386–391 (2020).
17. Duris, J. et al. Tunable isolated attosecond X-ray pulses with gigawatt peak power from a free-electron laser. *Nat. Photonics* **14**, 30–36 (2020).
18. Emma, P. et al. Femtosecond and subfemtosecond X-ray pulses from a self-amplified spontaneous-emission based free-electron laser. *Phys. Rev. Lett.* **92**, 074801 (2004).
19. Marinelli, A. et al. Optical shaping of X-ray free-electron lasers. *Phys. Rev. Lett.* **116**, 254801 (2016).
20. Behrens, C. et al. Few-femtosecond time-resolved measurements of X-ray free-electron lasers. *Nat. Commun.* **5**, 3762 (2014).
21. Ding, Y. et al. Generating femtosecond X-ray pulses using an emittance-spoiling foil in free-electron lasers. *Appl. Phys. Lett.* **107**, 191104 (2015).
22. Zholents, A. A. & Penn, G. Obtaining attosecond x-ray pulses using a self-amplified spontaneous emission free electron laser. *Phys. Rev. Spec. Top. Accel. Beams* **8**, 050704 (2005).
23. Guetg, M. W. et al. Generation of high-power high-intensity short X-ray free-electron-laser pulses. *Phys. Rev. Lett.* **120**, 014801 (2018).
24. Ding, Y. et al. Beam shaping to improve the free-electron laser performance at the Linac Coherent Light Source. *Phys. Rev. Accel. Beams* **19**, 100703 (2016).
25. Huang, S. et al. Generating single-spike hard X-ray pulses with nonlinear bunch compression in free-electron lasers. *Phys. Rev. Lett.* **119**, 154801 (2017).
26. Marinelli, A. et al. Experimental demonstration of a single-spike hard-X-ray free-electron laser starting from noise. *Appl. Phys. Lett.* **111**, 151101 (2017).
27. Giannessi, L., Musumeci, P. & Spampinati, S. Nonlinear pulse evolution in seeded free-electron laser amplifiers and in free-electron laser cascades. *J. Appl. Phys.* **98**, 043110 (2005).
28. Bonifacio, R., De Salvo Souza, L., Pierini, P. & Piovella, N. The superradiant regime of a FEL: analytical and numerical results. *Nucl. Instrum. Methods Phys. Res. A* **296**, 358–367 (1990).
29. Bonifacio, R., Piovella, N. & McNeil, B. W. J. Superradiant evolution of radiation pulses in a free-electron laser. *Phys. Rev. A* **44**, R3441–R3444 (1991).
30. Yang, X., Mirian, N. & Giannessi, L. Postsaturation dynamics and superluminal propagation of a superradiant spike in a free-electron laser amplifier. *Phys. Rev. Accel. Beams* **23**, 010703 (2020).
31. Watanabe, T. et al. Experimental characterization of superradiance in a single-pass high-gain laser-seeded free-electron laser amplifier. *Phys. Rev. Lett.* **98**, 034802 (2007).
32. Giannessi, L. et al. High-order-harmonic generation and superradiance in a seeded free-electron laser. *Phys. Rev. Lett.* **108**, 164801 (2012).
33. Giannessi, L. et al. Superradiant cascade in a seeded free-electron laser. *Phys. Rev. Lett.* **110**, 044801 (2013).
34. Svelto, O. & Hanna, D. C. *Principles of Lasers* (Springer, 2010).
35. Allaria, E., Ninno, G. D. & Spezzani, C. Experimental demonstration of frequency pulling in single-pass free-electron lasers. *Opt. Express* **19**, 10619–10624 (2011).
36. Helml, W. et al. Ultrashort free-electron laser X-ray pulses. *Appl. Sci.* **7**, 915 (2017).
37. Mitzner, R. et al. Direct autocorrelation of soft-x-ray free-electron-laser pulses by time-resolved two-photon double ionization of He. *Phys. Rev. A* **80**, 025402 (2009).
38. Svetina, C. et al. The Low Density Matter (LDM) beamline at FERMI: optical layout and first commissioning. *J. Synchrotron Radiat.* **22**, 538–543 (2015).
39. Zangrando, M. et al. Recent results of PADReS, the Photon Analysis Delivery and REduction System, from the FERMI FEL commissioning and user operations. *J. Synchrotron Radiat.* **22**, 565–570 (2015).
40. Reiche, S. GENESIS 1.3: a fully 3D time-dependent FEL simulation code. *Nucl. Instrum. Methods Phys. Res. A* **429**, 243–248 (1999).
41. Labat, M. et al. Pulse splitting in short wavelength seeded free electron lasers. *Phys. Rev. Lett.* **103**, 264801 (2009).
42. De Ninno, G., Mahieu, B., Allaria, E., Giannessi, L. & Spampinati, S. Chirped seeded free-electron lasers: self-standing light sources for two-color pump-probe experiments. *Phys. Rev. Lett.* **110**, 064801 (2013).
43. Mahieu, B. et al. Two-colour generation in a chirped seeded free-electron laser: a close look. *Opt. Express* **21**, 22728–22741 (2013).
44. Bonifacio, R., Pellegrini, C. & Narducci, L. M. Collective instabilities and high-gain regime in a free electron laser. *Opt. Commun.* **50**, 373–378 (1984).

Methods

Free-electron laser parameters and setup. The experiments were carried out at the FERMI FEL-2 line[45] during three experimental sessions, labelled A, B and C. The beam/undulator parameters changed slightly from one session to another and are listed in Table 1. All the data presented in the paper, except for those in Fig. 5, were collected during session A. The data in Fig. 5 were instead acquired during two succeeding experimental shifts, with parameters listed in columns B and C, respectively. The latter were dedicated to an attempt to measure directly the gain bandwidth in the final amplifier (Supplementary Information) that led to the observation of the frequency pulling in SRC mode.

The electron beam parameters and phase space may be considered uniform over the range of the seeded region. The beam performance in terms of energy spread improved over time as a result of our efforts in mitigating the microbunching instability growth along the linac. During sessions B and C the value of the slice energy spread is indeed below the sensitivity of the dipole/radiofrequency deflector system used for this measurement (~80 keV). The transverse emittances represent the figures for the expected 'slice' values of this parameter at the seeded region. These values are inferred from a measurement in the low-energy part of the linac at the laser heater position (~100 MeV), where the effects of transverse wakes and coherent synchrotron radiation are better controlled. The measurements of the projected emittances carried out in front of the undulator are about 40% larger, but this is the result of wakes along the linac correlating the transverse position with the longitudinal along the beam. The emittances increased slightly over time owing to transverse offsets of the photoinjector laser spot on the cathode surface, which we introduce periodically to preserve the effective cathode quantum efficiency. The seed energy reported is larger in SRC mode than in HGHG mode to induce saturation earlier along the FEL cascade. The listed energy is the measured value, typically larger than the value used in the simulation because of the ideal mode shape and alignment of the simulated model.

The FERMI FEL-2 beamline shown in Fig. 1 consists of 13 undulators of the three different types listed in Table 1. The first modulator is a planar undulator and all the other undulators are Apple-II-type undulators, used in right-circular polarization for this experiment. The undulator strength for each undulator can be calculated depending on the configurations shown in Fig. 1, on the seed wavelength and on the combination of harmonics as listed in Table 1.

The pulse energy in Fig. 3 is measured by the FERMI ionization monitors by interposing a 100-nm-thick zirconium filter to eliminate the seed and the light emitted by the first stages. A filter attenuation of 55 ± 5% (ref. [46]) accounting for zirconium and oxides was included for determining the energy absolute values at the source.

Autocorrelation measurement. A direct measurement of the duration of FEL pulses is possible by cross-correlation with a calibrated optical source, by streaking, or by autocorrelation; these aspects have been reviewed in refs. [11,36,47]. Autocorrelation in the EUV/soft-X-ray regime is more difficult and less flexible than cross-correlation, but for such short pulses it is the most reasonable option and was adopted here. The measurement was realized by splitting and recombining the FEL pulse with the FERMI split-and-delay line auto-correlator/delay-creator (AC/DC)[48] and by monitoring the (energy-resolved) signal of two-photon ATI of argon at the low-density matter beamline[38].

Table 1 | Electron beam, seed and undulator parameters

Beam/seed parameters	A (SRC/HGHG)	B (SRC)	C (HGHG)
Beam energy (MeV)	750 ± 1	900 ± 1	940 ± 1
Peak current (A)	700 ± 30		
Energy spread (keV)	130 ± 30	<80	<80
Transverse emittance (mm mrad)	1.2 ± 0.3	1.5 ± 0.5	1.5 ± 0.5
Beam size (μm)	90 ± 10	92 ± 10	90 ± 10
Seed wavelength (nm)	264.4 ± 0.1	266.2 ± 0.1	250.0 ± 0.1
Seed energy (μJ)	40 ± 2	44 ± 2	31 ± 2
Seed duration (fs)	55 ± 5	55 ± 5	90 ± 5
Harmonics up-shifts	3×2×3 / 6×3	3×2×3	7×3
Undulator parameters (SRC/HGHG, see Fig. 1)			
Undulator		Period (cm)	Periods
MOD1		10.036	30
RAD1 and RAD2/RAD1 and MOD2		5.52	42
RAD3/RAD2		3.48	66

A magnetic bottle electron spectrometer, with a retardation lens system derived from the design of Eland et al.[49], was installed with a configuration allowing the detection of alternatively electrons or ions; the spectrometer design has been presented previously (see refs. [11,50]). The electron time-of-flight signal was acquired shot-to-shot with a fast digitizer (Model V1751, 8 channels, 10 bit, 1 gigasample per second, CAEN) and stored for post-processing. Argon gas was injected into the source chamber using an Even–Lavie pulsed valve and admitted into the detector chamber through a skimmer (Model 2, Beam Dynamics); the parameters of the expansion are: nozzle diameter 100 μm; nominal opening time 21.5 μs; stagnation pressure 20 bar; skimmer diameter 3 mm; nozzle–detector distance ≈ 500 mm; nozzle–skimmer distance ≈ 140 mm.

The focal shape and position of the FEL beam were first imaged onto a YAG screen inserted in the interaction region (HI-RES YAG, resolution 7 μm), then optimized using a Shack–Hartmann wavefront sensor; the end-station was mounted on rails and was displaced back-and-forth by a few millimetres along the FEL beam while monitoring the target two-photon signal to optimize the relative position of the FEL beam focus and the spectrometer axis. The gas jet, the FEL beam and the spectrometer axis are mutually perpendicular, with the first two lying in a horizontal plane and the last along the vertical direction. An example of the detected high kinetic energy spectrum is shown in Fig. 2c. For the measurement of the ATI signal, the retardation voltage of the magnetic bottle was set to 70 V to exclude the strong single-photon component falling at lower kinetic energies (Ar 3*s*: 55.3 eV; Ar 3*p*: 68.7 eV). The bias voltage, or gain, of the electron multiplier was set to 1,900 V, resulting in single-electron peaks with average height of 80 mV. The flight tube region is ~2 m long, resulting in a time of flight of ~370 ns for 153 eV electrons (kinetic energy before retardation by 70 V).

The AC/DC was then inserted and the time-zero position (equal length of the two arms) was determined by observing the appearance of interference fringes on a YAG screen imaging the two unfocused beams after the delay line. Finally, the focal spots of the two paths were imaged onto HI-RES YAG and made to coincide by fine tuning the delay-line alignment. While the movement of the delay line caused a slight loss of spatial overlap, we verified that this was reproducible over the scan range used for the present experiment (which was in any case very small: at most 2 mm of travel, or 73 fs) and implemented a look-up table to automatically correct it.

To extract the delay-time-dependent ATI yield from the electron spectra, the single-shot analogue traces were software discriminated a posteriori by applying a threshold based on the baseline noise level and determining for each electron detection event the time of arrival (given by the centre of mass of the peak) and the peak integral. The ATI detection counting rate varied between 0.025 and 0.05 counts per shot within the region-of-interest (ROI) of 365–425 ns depending on the AC/DC delay setting. The ATI yield can be determined as the number of counts in the ROI, the integral of the discriminated peak in the ROI or simply the integral of the analogue trace in the ROI. All these approaches gave very similar yields, so the autocorrelation yield as a function of the delay could be obtained from their average normalized to the value at zero delay. The yield uncertainty is given by the counting statistics. The autocorrelation trace for both the SRC and the HGHG FEL configurations is shown in Fig. 2.

Data availability

Source data are provided with this paper. The data that support the plots within this paper and other findings of this study are available from the corresponding author upon reasonable request.

Code availability

The simulation reported in Fig. 4 was carried out with version 2 and version 4 of the code GENESIS 1.3 available at http://genesis.web.psi.ch and https://github.com/svenreiche/Genesis-1.3-Version4.

References

45. Allaria, E. et al. Two-stage seeded soft-X-ray free-electron laser. *Nat. Photonics* **7**, 913–918 (2013).
46. Henke, B. L., Gullikson, E. M. & Davis, J. C. X-ray interactions: photoabsorption, scattering, transmission, and reflection at $E = 50–30{,}000$ eV, $Z = 1–92$. *At. Data Nucl. Data Tables* **54**, 181–342 (1993).
47. Düsterer, S. et al. Development of experimental techniques for the characterization of ultrashort photon pulses of extreme ultraviolet free-electron lasers. *Phys. Rev. Spec. Top. Accel. Beams* **17**, 120702 (2014).
48. Roling, S. & Zacharias, H. in *Synchrotron Light Sources and Free-Electron Lasers* (eds Jaeschke, E. et al.) 891–925 (Springer, 2014).
49. Eland, J. H. D. et al. Complete two-electron spectra in double photoionization: the rare gases Ar, Kr, and Xe. *Phys. Rev. Lett.* **90**, 053003 (2003).
50. Squibb, R. J. et al. Acetylacetone photodynamics at a seeded free-electron laser. *Nat. Commun.* **9**, 63 (2018).

Acknowledgements
We acknowledge S. Reiche for helpful discussions on bandwidth issues in the simulation of a multistage cascade in GENESIS 1.3. We are also grateful to the whole FERMI team for the dedicated work and support during this experiment.

Author contributions
N.S.M., S.S. and L.G. conceived the idea of the experiment. C.C. and T.M. conceived the ATI autocorrelation measurement scheme. N.S.M., S.S., E.A., L.B., G.D.N., S.D.M., G.P., P.R., C.S., G.G., M.T., X.Y. and L.G. contributed to the machine operation and tuning for the experiment. S.S., N.S.M. and F.S. simulated the FEL SRC dynamics in the experimental conditions. S.S. and F.S. investigated the energy detuning and the frequency-pulling effect. M.B.D. and A.D. tuned the seed laser for short-pulse operation. N.M., M.M., L.R. and M.Z. designed, aligned and operated the split-and-delay line; O.P., K.C.P., T.M., M.D.F., R.J.S. and C.C. operated the magnetic bottle electron spectrometer, acquired and analysed the cross-correlation data. T.M. and M.D.F. developed the analysis tools used during beam time. N.S.M., C.C., K.C.P. and L.G. wrote the manuscript, which was discussed and agreed by all the coauthors.

Competing interests
The authors declare no competing interests.

Additional information
Supplementary information The online version contains supplementary material available at https://doi.org/10.1038/s41566-021-00815-w.

Correspondence and requests for materials should be addressed to L.G.

Peer review information *Nature Photonics* thanks Agostino Marinelli and the other, anonymous, reviewer(s) for their contribution to the peer review of this work.

Reprints and permissions information is available at www.nature.com/reprints.